International Journal of Heat and Mass Transfer 158 (2020) 119850

Contents lists available at ScienceDirect

International Journal of Heat and Mass Transfer

journal homepage: www.elsevier.com/locate/hmt

Molecular dynamics studies of bubble nucleation on a grooved substrate

Yu-Jie Chen[a], Bo Yu[b,*], Yu Zou[b], Bing-Nan Chen[b,c], Wen-Quan Tao[a]

[a] Key Laboratory of Thermo-Fluid Science and Engineering of MOE, School of Energy and Power Engineering, Xi'an Jiaotong University, Xi'an Shaanxi 710049, China
[b] School of Mechanical Engineering, Beijing Key Laboratory of Pipeline Critical Technology and Equipment for Deepwater Oil & Gas Development, Beijing Institute of Petrochemical Technology, Beijing 102617, China
[c] College of Environmental and Energy Engineering, Beijing University of Technology, 100 Pingleyuan Chaoyang District, Beijing 100124, China

ARTICLE INFO

Article history:
Received 19 December 2019
Revised 13 April 2020
Accepted 21 April 2020
Available online 30 June 2020

Keywords:
Bubble nucleation
Grooved substrate
Wettability
Molecular dynamics simulation

ABSTRACT

The classical heterogeneous nucleation theory explains that the groove in the substrate is a desirable place to breed a bubble nucleus. However, the existing research method cannot reproduce the nucleation process. Therefore, in the present study, the molecular dynamics simulation method is conducted to investigate the bubble nucleation on grooved substrates with different wettability. The simple L-J liquid argon is heated by the platinum grooved substrate, whose temperature is controlled by Langevin thermostat. Results show that the groove has significant impacts on bubble nucleation from two aspects: improve thermal energy transfer efficiency and support an initial bubble nucleus. For the substrate with a hydrophilic groove, a visible bubble nucleus generates on the groove region from nothing because of liquid in there obtaining more thermal energy than that on the smooth region within the same time. Moreover, the nucleation rate is improved with the increase of groove hydrophilicity. On the other hand, for the substrate with a hydrophobic groove, some residual gases form an initial bubble nucleus at the initial moment of the nonequilibrium simulation stage, and it takes some time to grow up. Furthermore, a method based on the competition between atomic potential energy and atomic kinetic energy is used to explain the formation of the bubble nucleus on the different wetting substrates. The present simulation study of bubble nucleation on the grooved substrate is another support for the classical heterogeneous nucleation theory.

1. Introduction

Bubble nucleation in nucleate boiling is a fundamental issue involving many disciplines, such as heat transfer, physics, and fluid mechanics [1–3]. It has attracted considerable attention in the researches of enhancing heat transfer in the past decades, especially with the rapid development of microelectronic technology [4]. The classical heterogeneous nucleation theory indicates that the groove in the heating surface is the most likely place to generate the bubble nucleus. Moreover, some studies of boiling on the heated surfaces with micro-machined artificial cavities have been conducted to enhance nucleate boiling efficiency [5]. However, the traditional methods are inapplicable to observe the bubble nucleation process in the micro-scale because of the restriction of time scale and space scale. The further understanding of the bubble nucleation process on a groove is needed to push forward the application of nucleate boiling in enhancing heat transfer.

The molecular dynamics simulation method basing on statistical mechanics is conducted to simulate the microscopic behavior of molecular motion and obtain the macro properties of the molecular system, and which is a valuable tool to study bubble nucleation [6]. Hens et al. [7] investigated the bubble nucleation on a smooth substrate surface with uneven temperatures. The results revealed that the bubble nucleation could be observed in the region with higher degrees of superheat. Nagayama et al. [8] studied the bubble nucleation behavior in a nanochannel. It was found that bubble nucleation behavior was significantly different from that on the smooth substrate with varying wettability. Homogeneous nucleation and heterogeneous nucleation respectively appeared on hydrophilic and hydrophobic substrates. Moreover, the inapplicability of the Young-Laplace equation in nanoscale was verified. Maruyama et al. [9] expanded the nanochannel gradually, and the heterogeneous nucleation successfully was visualized under different interfacial wettability conditions. Yamamoto et al. [10] investi-

* Corresponding author.
E-mail address: yubobox@vip.163.com (B. Yu).

https://doi.org/10.1016/j.ijheatmasstransfer.2020.119850
0017-9310/

gated the initial stage of bubble nucleation on smooth substrates with uneven superheat and surface wettability, respectively. Under these two conditions, the bubble nucleus successfully generated in the vicinity of the substrate, and the inception time of nucleation was related to substrate wettability and superheat. She et al. [11] analyzed the bubble nucleation process on a substrate with a groove, which enhanced the formation of the bubble nucleus. It was found that the hydrophilic substrate had a better performance in bubble nucleation, while no bubble nucleus formed on a strongly hydrophobic substrate. Liu et al. [12] studied the process of bubble nucleation on a rough hydrophobic substrate, and the thermodynamic integration method was applied to quantitatively evaluate the change of free energy during the phase transition process. Zhou et al. [13] investigated the bubble nucleation of liquid argon over patterned surfaces with different wettability. Results showed that the position of bubble nucleation tended to move from the hydrophobic region to the hydrophilic region with the increase of substrate temperature. Chen et al. [14–17] explored bubble nucleation phenomena on the substrates with different wettability and nanostructure conditions. It was found that the substrate inhomogeneity had a significant impact on bubble nucleation.

The above studies provide significant insights into heterogeneous nucleation under different conditions, and the effects of substrate wettability, groove, and convex nanostructure on bubble nucleation have been thoroughly discussed. However, the formation mechanism of the bubble nucleus did not be illustrated clearly at the nanoscale, which hinders the further development of nucleate boiling in the practical application. The classical heterogeneous nucleation theory explains that the groove in the heating substrate is conducive to the formation of bubble nucleus because of the following two reasons: one is the liquid in the groove obtaining more thermal energy than that on the plane within the same time, another is some residual gases in groove becoming the initial bubble nucleus [18]. For the simple L-J liquid, the evaporation of atoms from the vapor-liquid interface can be viewed as an escape from a potential energy well [19]. We can easily associate that enough kinetic energy is the trigger of escape, and the competition of atomic potential energy and atomic kinetic energy may be a valuable idea to explain the advantage of the groove in bubble nucleation. Therefore, based on this idea, the molecular dynamics simulation method is conducted to investigate the formation mechanism of a bubble nucleus on a grooved substrate with different wettability from the two mentioned perspectives of classical nucleation theory in the present study.

2. Simulation system and method

The simulation box is illustrated in Fig. 1, which is a cubic box with a size of 14.9 nm (x) × 14.9 nm (y) × 82.1 nm (z). The purple argon (Ar) and light blue platinum (Pt) are selected as the simulation mediums of liquid and metal substrate, respectively. Ten layers of light blue platinum atoms are placed at the bottom with the arrangement of face-centered cubic structures (FCC (1 1 1)) [20]; 40000 liquid argon atoms are placed on the substrate surface with a density of 1.367 g/cm³; the vapor argon atoms evaporate from the liquid surface into the upper vapor region during the equilibrium simulation process. It is noteworthy that the three layers of platinum atoms at the bottom are set as the heat source, whose temperature is controlled by a Langevin thermostat. A periodic boundary is applied to the x-direction and y-direction, and the argon atoms come back to the simulation box from one side when it leaves on the opposite side. On the other hand, a reflecting wall is applied to the z-direction because of the existence of a metal substrate at the bottom. The argon atoms reflect from the top boundary without any losses of energy and momentum.

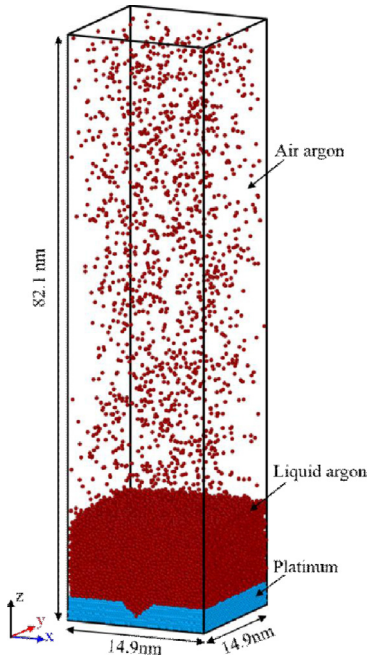

Fig. 1. Initial configuration of the simulation system.

Table 1
Lennard-Jones parameters for Ar-Ar, Pt-Pt [21]

Interaction type	ε/eV	σ/nm
Ar-Ar	0.0104	0.34
Pt-Pt	0.52	0.2475

The interaction potentials of Ar-Ar and Pt-Pt are described by the Lennard-Jones (L-J) potential.

$$\phi_{Ar-Ar}(r) = 4\varepsilon_{Ar-Ar}\left[\left(\frac{\sigma_{Ar-Ar}}{r}\right)^{12} - \left(\frac{\sigma_{Ar-Ar}}{r}\right)^{6}\right] \tag{1}$$

$$\phi_{Pt-Pt}(r) = 4\varepsilon_{Pt-Pt}\left[\left(\frac{\sigma_{Pt-Pt}}{r}\right)^{12} - \left(\frac{\sigma_{Pt-Pt}}{r}\right)^{6}\right] \tag{2}$$

where ε and σ express the energy parameter and length parameter, respectively. The exact values for these parameters are listed in Table 1.

The interaction potential of Ar-Pt is related to the interfacial wettability of solid-liquid. Thus a new form of the L-J potential is presented, as shown in Eq. (3). This new potential formula is a combination of the potential models used by Din [22] and Barrat [23].

$$\phi_{Pt-Ar}(r) = 4\varepsilon_{Pt-Ar}\left[\left(\frac{\sigma_{Pt-Ar}}{r}\right)^{12} - \beta\left(\frac{\sigma_{Pt-Ar}}{r}\right)^{6}\right] \tag{3}$$

$$\varepsilon_{Pt-Ar} = \alpha\sqrt{\varepsilon_{Pt}\varepsilon_{Ar}} \tag{4}$$

$$\sigma_{Pt-Ar} = \frac{\sigma_{Pt} + \sigma_{Ar}}{2} \tag{5}$$

where ε_{Pt-Ar} and σ_{Pt-Ar} are calculated by Eqs. (4) and (5) basing on the Lorentz-Berthelot combining rule [24]. β and α are used to adjust the substrate wettability, and their values are presented in Table 2.

The present study is conducted by a Large-scale Atomic/Molecular Massively Parallel Simulator (LAMMPS) [25], which is a popular open-source software for molecular dynamics simulation developed by the Sandia National Laboratory. During the simulation process, the cut-off radius $r_c = 3.5\sigma_{Ar}$ and time step

Table 2
Different interfacial wettability of solid-liquid based on α and β [8]

Surface wettability	α	β	Contact angle
Weak hydrophilicity	0.14	1	0°
Strong hydrophilicity	1	1	0°
Strong hydrophobicity	0.14	0.1	180°

$\Delta t = 5fs$ are set to reduce computation time, and the position and velocity of each atom are updated by a Velocity-Verlet algorithm [26]. The simulations in the present study include two main stages: preparation and nonequilibrium. In the preparation stage, a 2.5 ns simulation in the canonical ensemble NVT (N is atom number, V is volume, T is temperature) is conducted to achieve an equilibrium stage at 90 K. In the nonequilibrium simulation stage, the temperature of heat-source is raised to 200 K (T/T_c=1.3, T_c is critical temperature) by the Langevin thermostat. An additional 5 ns nonequilibrium simulation in the microcanonical ensemble NVE (N is atom number, V is volume, E is energy) is conducted to study the bubble nucleation process on the grooved substrate. In both stages, the simulation data are output every 100 time-steps, and the atom trajectories are visualized by the open visualization tool OVITO [27].

3. Results and discussion

Based on the above simulation system and methods, in this section, the bubble nucleation processes on the grooved substrates with different wettability are studied to make a comparison with the classical heterogeneous nucleation theory in the formation of a bubble nucleus. Moreover, the formation mechanism of the bubble nucleus on a grooved substrate is illustrated from the competition of atomic kinetic energy and atomic potential restriction.

3.1. The comparison of bubble nucleation on grooved substrates with different wettability

The heat transfer efficiency of solid-liquid increases with the enhancement of substrate hydrophilicity [17]. If the hydrophilicity of the groove region is stronger than that of the smooth region, bubble nucleation may happen on the groove [10,13]. On the other hand, some residual gases in the hydrophobic groove were found in our previous study [14]. Therefore, in the present study, strong hydrophobicity, weak hydrophilicity, and strong hydrophilicity are taken as the representatives to study bubble nucleation on a grooved substrate. The wettability configurations of grooved substrates are illustrated in Table 3.

Fig. 2 illustrates the representative snapshots of bubble nucleation processes on the grooved substrates with different wettability. The bubble nucleation phenomena are different between the hydrophilic groove and hydrophobic groove. For Cases A and B with a hydrophilic groove, a visible bubble nucleus turns up from nothing on the groove region at about 4100ps and 3000ps, respectively, and the bubble nucleus continues to grow up with the increasing time. It can be concluded that the hydrophilicity difference between the groove region and smooth region is not the cause of bubble nucleation, but the incipient nucleation time is shortened with the increase of hydrophilicity. Besides, the hydrophilic groove surface is covered with a layer of argon atoms all the time, which is common in the study of boiling and evaporation in nanoscale [28]. For Case C with a hydrophobic groove, some gases remain in the groove and become the initial bubble nucleus, which begins to grow up further at about 5100 ps. On the other hand, the nucleation rate and critical nucleus size are the concerned quantities in bubble nucleation study. Therefore, based on the method of mean first-passage times (MFPT), further comparisons between different wetting substrates in these two parameters are made. The procedure is illustrated as follows.

Table 3
Configuration of different simulation cases

Simulation case	Wettability of groove region	Wettability of smooth region
Case A	Weak hydrophilicity	Weak hydrophilicity
Case B	Strong hydrophilicity	Weak hydrophilicity
Case C	Strong hydrophobicity	Weak hydrophilicity

In an activated process, the rate of barrier crossing is related to the mean first-passage times, which is defined as the average elapsed time until the system starting at point x_0 leaves a prescribed domain [a, b] for the first time [29, 30].

$$\tau(x_0; a, b) = \int_{x_0}^{b} \frac{1}{D_0} dy \exp[\beta U(y)] \int_{a}^{y} dz \exp[-\beta U(z)] \tag{6}$$

where D_0 is the generalized diffusion coefficient, $U(y)$ is the free energy barrier for nucleation, x_0 is the initial position, and β=$1/kT$ is the inverse of the product of Boltzmann constant k and temperature T. For most cases of interest, the boundary conditions are typically reflecting at point a and absorbing at point b. The average time for the system to reach b for the first time can be obtained by fixing a given starting point. It is worth stressing that the shape of the bubble nucleus in the present study likes a cylinder under the effect of the groove crossing the substrate surface along the y-direction. Therefore, in the present study, the bubble nucleus volume is set as the concerned parameter in the calculation of the nucleation rate, corresponding to the parameter b.

Under reasonably high barriers, the MFPT of volume b can be evaluated by the method of steepest descent, and it is described by the following expression [31]:

$$\tau(b) = \frac{\tau_J}{2}\{1 + erf[(b - x^*)c]\} \tag{7}$$

where $\tau_J = \frac{1}{JV}$ is the inverse of the nucleation rate in unit volume, $erf(x) = 2/\sqrt{\pi}\int_0^x e^{-x^2}dx$ is the error function, $c = \sqrt{\frac{|U''(x^*)|}{2kT}}$ is the local curvature around the top of the barrier curve, and x^* is the critical volume of the bubble nucleus. It is attractive that the nucleation rate and the critical nucleus volume can be obtained by merely fitting the results of MFPT in the MD simulation to this simple expression.

Next, what we concern about is how to obtain the MFPT from the MD simulations. Firstly, during the simulation process, the volume b of the largest bubble nucleus is noted at the regular time step (1000 time-steps in the present study), and the corresponding time $\tau_i(b)$ is recorded as well. Then, the mean first-passage time $\tau(b)$ for each volume b is obtained by averaging $\tau_i(b)$ over several repetitions of the MD simulations with different initial configurations. It is noteworthy that only one bubble nucleus exists in the simulation box during the nucleation process, and that is the largest one at the regular time step, as shown in Fig. 2. On the other hand, in the present study, the heterogeneous bubble nucleation is induced by the hot substrate, and there is no significant difference in the bubble size between the repeated MD simulations at the regular time step. On the contrary, the bubble nucleation process is arbitrary in the MD study of the homogeneous nucleus [31]. Therefore, in the present study, 20 repeated MD simulations are conducted to obtain the MFPT for the cases with different wetting substrates, respectively.

Fig. 3 shows the trends of mean first-passage time with bubble nucleus volume for the cases with different wetting substrates. The fits work well with Eq. (7) for all cases, and the mean first-passage time reaches a plateau $\tau_J = \frac{1}{JV}$. It is noteworthy that the

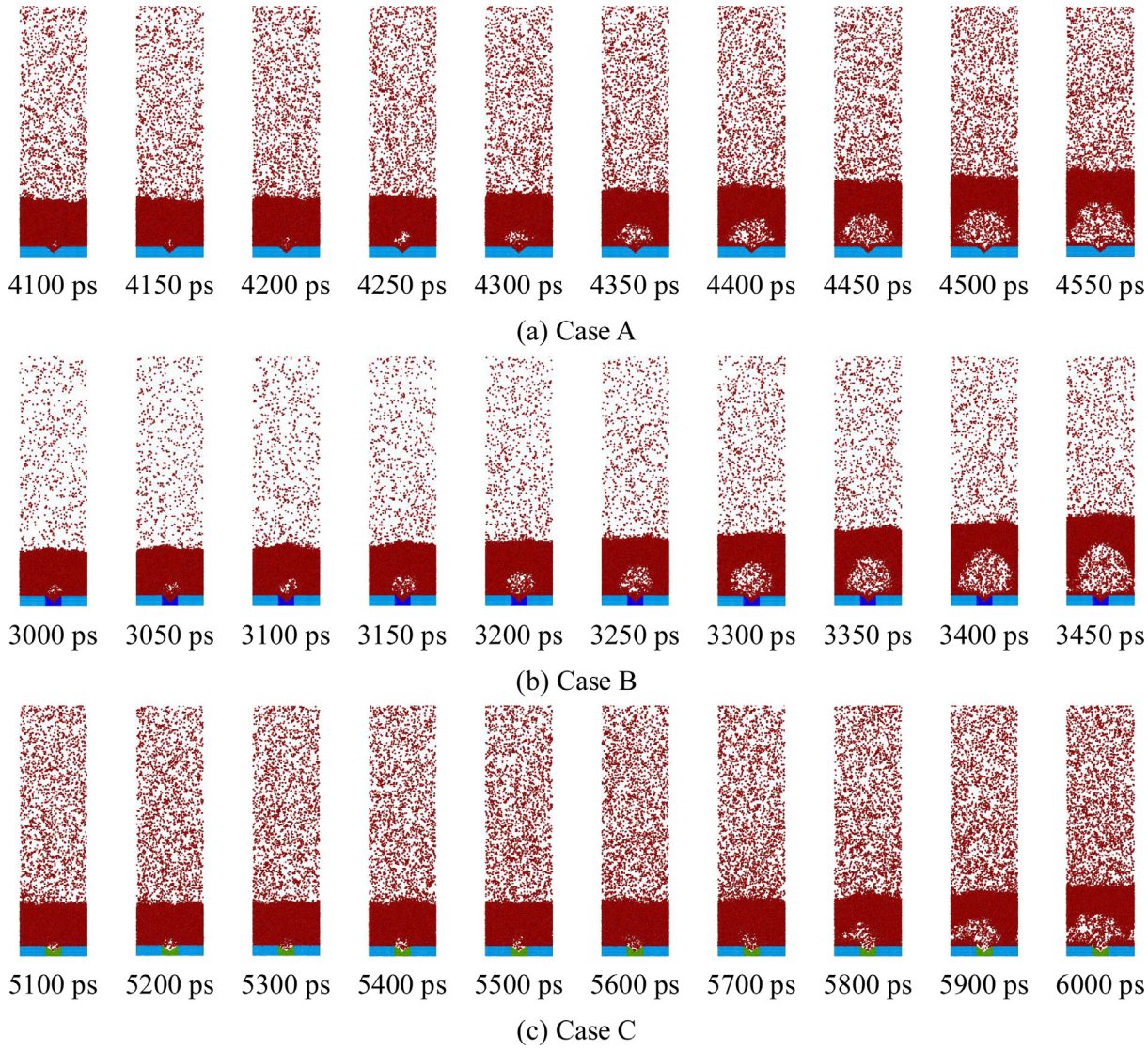

Fig. 2. Representative snapshots of bubble nucleation process on the grooved substrate with different wettability.

bubble nucleation (hydrophilic groove) or bubble nucleus growth (hydrophobic groove) needs a long waiting time, and the thermal energy cumulation of liquid atoms in this period causes the quick growth of newborn bubble nucleus or initial bubble nucleus after some time. As a result, the trends of mean first-passage time for the cases with wetting substrates lack the first half part to fit with Eq. (7). The volume of the liquid region is 2250 nm^3 in the present study. Finally, the nucleation rates of 0.00025 $ns^{-1}\bullet nm^{-3}$, 0.00063 $ns^{-1}\bullet nm^{-3}$, and 0.00014 $ns^{-1}\bullet nm^{-3}$ for Cases A, B, and C are obtained, respectively. The hydrophilic case shows a higher nucleation rate than the hydrophobic one, and this trend is different from the classical heterogeneous nucleation theory. The reason for that is illustrated in the following part.

The critical volume of the bubble nucleus is derived from the fitting results. The nucleation rate is in inverse proportion to the time from the initial moment to the transition state of reaching the critical volume [30, 32].

$$J = \frac{1}{2\tau(x^*)V} \tag{8}$$

where the factor 1/2 comes from the fact that, at the top of the barrier, the system has a 50% chance of falling to either side.

For Case C, the critical volume of the bubble nucleus is 35.16 nm^3, which is bigger than the initial one at the beginning moment of the nonequilibrium simulation stage. The initial bubble nucleus needs to absorb thermal energy to break the energy barrier and grow up further. However, the exchange efficiency of thermal energy is very low between the strongly hydrophobic groove and the liquid on it. As a result, the liquid on the strongly hydrophobic groove can only absorb thermal energy from that on the hydrophilic region to break the energy barrier of critical volume, and it costs much time. On the other hand, the critical volumes of bubble nucleus only are 3.75 nm^3 and 0.16 nm^3 for Cases A and B, respectively. The critical volume of the bubble nucleus on the hydrophilic groove is so small that once the bubble nucleus turns up, it will exceed the critical size quickly and grow up further. Namely, the incipient nucleation moment is near the transition state. As a result, the hydrophilic groove has an advantage over the hydrophobic groove in the nucleation rate by comparison.

The nucleation kinetics can be described by the Fokker-Planck (FP) equation [31,33,34].

$$\partial P(x,t) = \frac{\partial}{\partial x}\left[D(x)e^{-\beta\Delta G(x)}\frac{\partial}{\partial x}\left(P(x,t)e^{\beta\Delta G(x)}\right)\right] \tag{9}$$

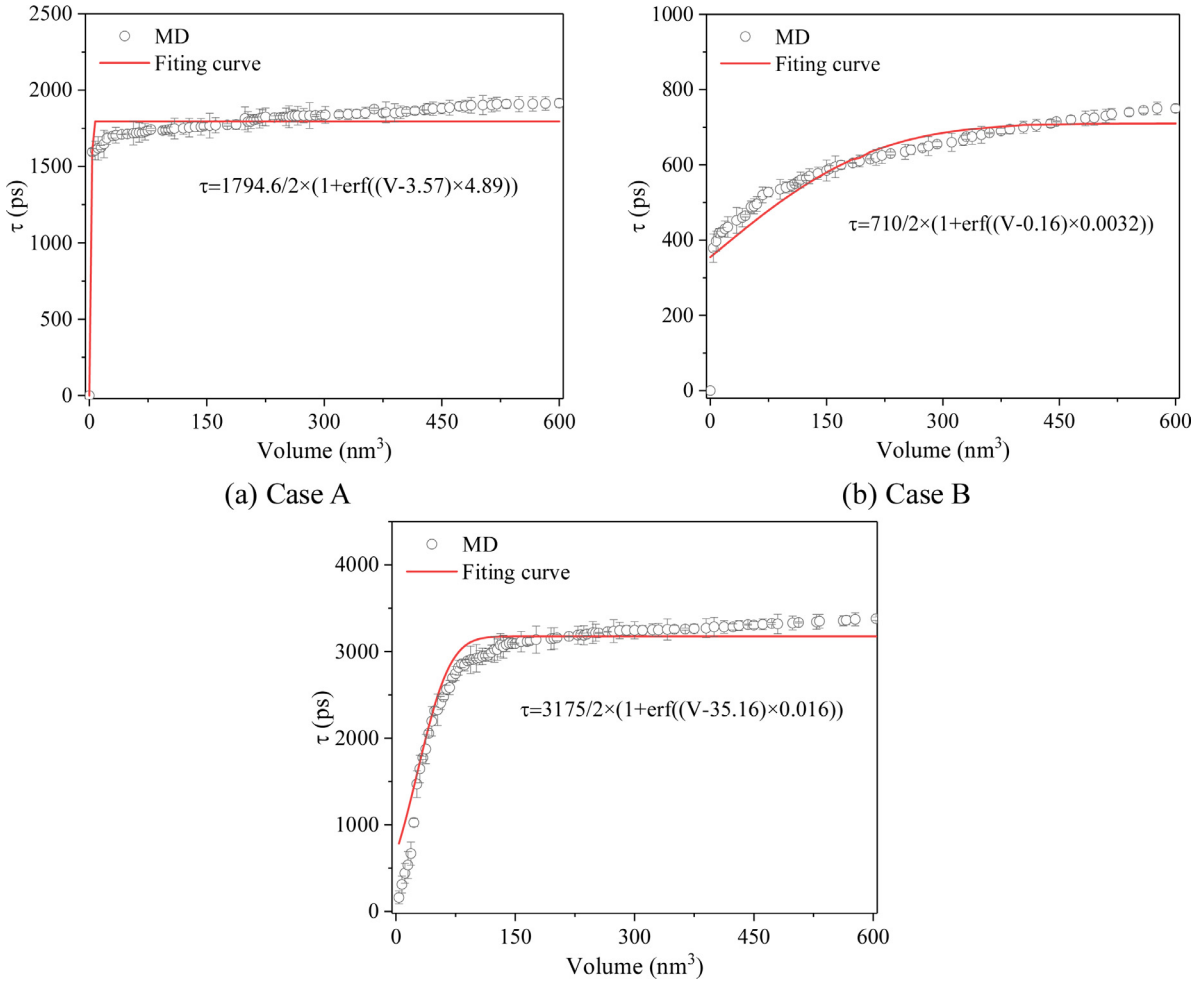

Fig. 3. Trends of mean first-passage time for the cases with wetting substrates.

where the effective diffusion $D(x)$ is the rate of bubble nucleus to a volume of x and is expressed as Eq. (10).

$$D_{\mathrm{CNT}}(x) = A(x^*)px^{2/3}/\sqrt{2\pi mkT} \tag{10}$$

where p is the vapor pressure and $A(x^*)$ the surface area of the critical bubble.

However, the temperature and pressure of the liquid are not constant in the present study of heterogeneous nucleation. Therefore, it is hard to obtain the theoretical results of the nucleation rate and critical nucleus size. On the contrary, for the homogeneous nucleation in the references [31,33,34], the temperature is fixed, and parameters p and $A(x^*)$ can be easily obtained [34]. As a result, a comparison can be made between the MD result and the theoretical result in the homogeneous nucleation.

In summary, the nucleation rate increases with the enhancement of groove hydrophilicity, and the critical bubble volume shows the opposite trend. More attractively, at the initial moment of nonequilibrium simulation stage, an initial bubble nucleus forms in the strongly hydrophobic groove, which is totally different from the bubble nucleation phenomenon in the hydrophilic groove. Fortunately, this difference can be used for the exploration of bubble nucleus formation from two perspectives of classical nucleation theory: some residual gases in groove becoming the initial bubble nucleus and the liquid in the groove obtaining more thermal energy to achieve nucleating [18]. Therefore, the next studies are divided into some parts according to the following questions:

(1) Whether the reason for the bubble nucleation on the grooved substrate with uniform weak hydrophilicity is the liquid atoms on the groove region obtain more thermal energy than that on the smooth region?
(2) For the hydrophilic groove, why the incipient nucleation time is shortened with the enhancement of groove hydrophilicity (nucleation rate improves with the enhancement of groove hydrophilicity)?
(3) Why some gases remain in the hydrophobic groove to form the initial bubble nucleus?
(4) The heat transfer efficiency between the strongly hydrophobic groove and the liquid atoms on it is very low. How can the initial bubble nucleus grow up from the hydrophobic groove by obtaining less thermal energy?

3.2. The introduction of the idea for explaining bubble nucleus formation on the grooved substrates with different wettability

To find the answers to the mentioned questions in Section 3.1, the study method is introduced firstly. On the macro scale, the barrier for the phase transition from liquid to vapor is the latent heat, which is overcome by absorbing enough thermal energy. This idea is available to explain the phase transition phenomenon at the macroscale, but not for the bubble nucleation at the microscale because of the restrictions of time scale and space scale.

On the microscale, the kinetic theory was proposed by Shen to illustrate homogeneous bubble nucleation [19]. In their study, the theory method is taken to analyze the potential energy well for the L-J liquid atoms evaporating from the vapor-liquid interface. In the study of Hill [35], for two monatomic molecules in phase space, if the relative kinetic energy of the molecules smaller than the negative of the potential energy of interaction, they were "bound" to each other and belonged to the same liquid cluster. For a group of monatomic molecules, a line was used to connect each “bound” molecules, and they were regarded as a part of one liquid cluster. However, in the present study, once bubble nucleation happens, many vapor atoms appear inside the bubble nucleus. Some vapor atoms inside the bubble nucleus may be “bound” with each other, but they should not be regarded as a part of the liquid. Therefore, based on the ideas of Shen and Hill, a modification is made to meet the requirement of the present study. If the average kinetic energy of a group of liquid atoms inside liquid exceeds their average potential restriction, the bubble nucleation is happening. On the other hand, the analogies can be made between latent heat and atomic potential restriction, thermal energy and atomic kinetic energy by combining the macro theory. Therefore, based on the above analysis and comparison, we believe that the formation mechanism of a bubble nucleus can be illustrated by the competition between atomic potential energy and atomic kinetic energy, and this idea is named “PK” norm (the letters “P” and “K” are the abbreviation of “Potential energy” and “Kinetic energy” respectively, and the combination “PK” implies the competition of atomic potential energy and atomic kinetic energy) in the present study. The idea of the “PK” norm is illustrated as follows.

Firstly, the idea of the “PK” norm is illustrated by the movements of two argon atoms, as shown in Fig. 4(a). Two argon atoms are put on a horizontal line at the initial moment. The Atom 1 is fixed at the original position all the time, and Atom 2 horizontally moving between Position 1 and Position 2 likes the simple harmonic motion under the potential restriction from Atom 1. The potential energy between Atom 1 and Atom 2 at Position 1 and Position 2 is the same, and the corresponding kinetic energy of Atom 2 is 0 at these two positions. Atom 2 is a part of the liquid in the present situation. Then, Atom 2 obtains a little thermal energy by an artificial mean, and its kinetic energy is increased slightly. The motion range of Atom 2 is changed to which from Position 3 to Position 4, as shown in Fig. 4(b). Although the moving distance of Atom 2 is increased, it cannot get rid of the potential restriction from Atom 1. Atom 2 still is a part of liquid as before. Furthermore, Atom 2 absorbs more energy, and its kinetic energy is larger than the potential restriction from Atom 1 at some moment. As a result, Atom 2 moves to Position 5 and continues to move freely along the opposite direction from Atom 1, as shown in Fig. 4(c). The potential energy between Atom 1 and Atom 2 is 0 when their distance is infinite. Thus Atom 2 keeps moving horizontally according to the law of energy conservation. Finally, Atom 2 is considered a part of the bubble nucleus.

Then, the idea of “PK” norm is further illustrated by a group of argon atoms inside the liquid, as shown in the red ring region in Fig. 5(a). This group of argon atoms moves within a tiny region at the initial moment of nonequilibrium simulation stage, and they are a part of the liquid. Then, they absorb thermal energy from the heating substrate, and their average kinetic energy is increased. Moreover, some of the thermal energy is converted to the potential energy (negative value) of this group of atoms, leading to the slight enlargement of the distance between different liquid atoms. Therefore, this group of atoms tends to move within a broader region, and the average potential restriction from the surrounding atoms to them is decreased at the same time, as shown in Fig. 5(b). However, this group of atoms still cannot get rid of their potential restriction, and no bubble nucleation happens. As time goes on, this group of atoms absorbs more and more thermal energy from the substrate, leading to a further decrease in average potential restriction and a further increase in average kinetic energy. At some moment, this group of atoms breaks their potential restriction, leading to the formation of a bubble nucleus, as shown in Fig. 5(c).

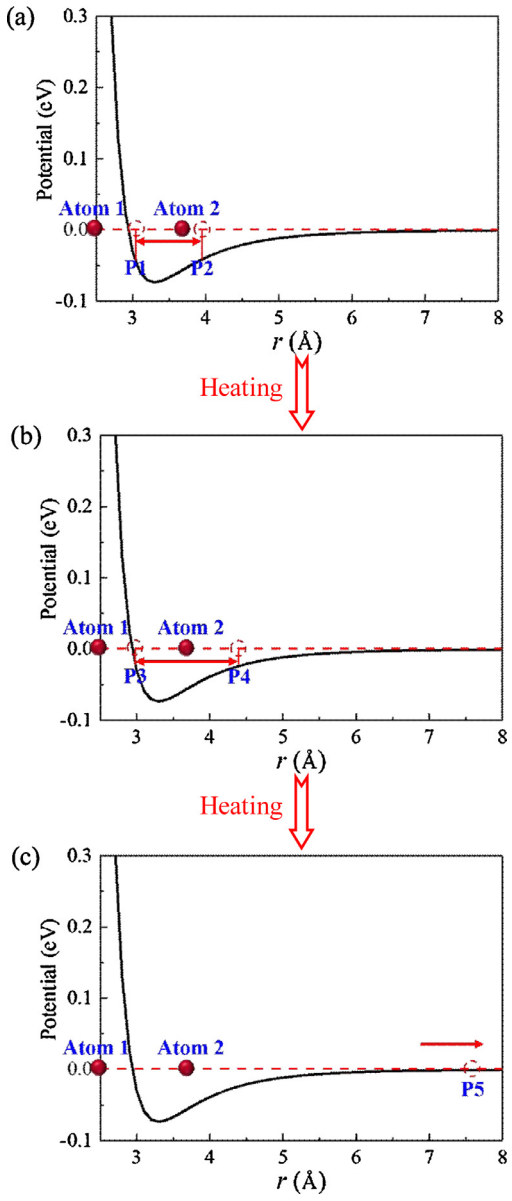

Fig. 4. Sketch map of the movement of one atom during the heating process.

3.3. The exploration of the reason for the bubble nucleation on the uniform hydrophilic grooved substrate

Based on the “PK” norm, the formation mechanism of a bubble nucleus on the uniform hydrophilic grooved substrate is illustrated in this subsection. The bottom half of the simulation box is divided into $30(x) \times 35(z)$ subregions with a size of 0.5 nm (x) × 149.0 nm (y) × 0.5 nm (z). The average kinetic energy of atoms in each subregion is calculated to obtain the kinetic energy contour, and the potential energy contour is obtained in the same way.

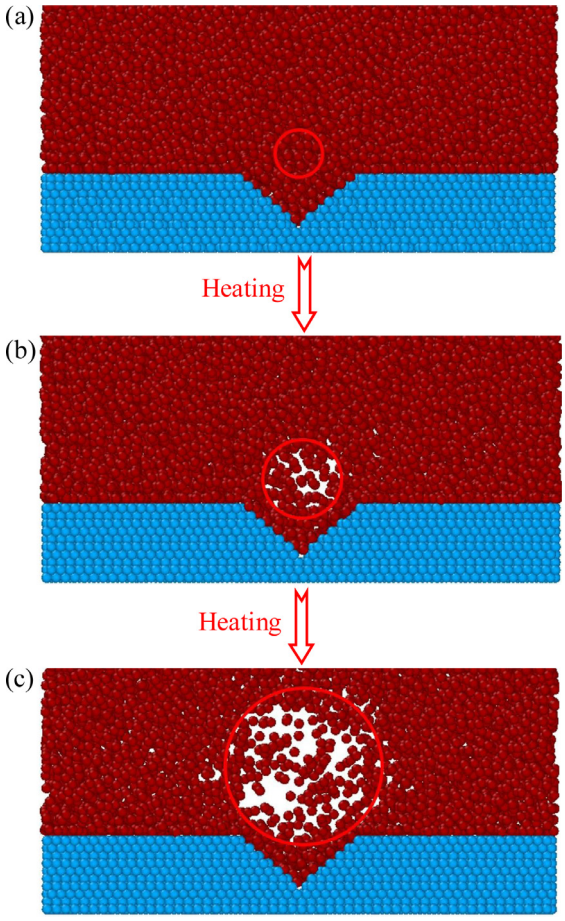

Fig. 5. Sketch map of the movement of a group of atoms during the heating process.

The temperature of heat-source is raised to 200 K by the Langevin thermostat at the beginning of the nonequilibrium stage (2500 ps). In Case A with uniform wettability, the liquid atoms in the vicinity of the grooved substrate directly obtain the thermal energy from the heating substrate. One part of the thermal energy is converted to the atomic kinetic energy, as shown in Fig. 6 (the solid-liquid interface at z=0 Å and the liquid-vapor interface at z=90 Å). The kinetic energy of liquid atoms is raised from the bottom to the top with the heating process, especially for the liquid atoms on the groove region, which have higher kinetic energy than the liquid atoms on the smooth region. It is worth stressing that the distribution of kinetic energy in the upper region is uneven because of the sparse distribution of vapor atoms. On the other hand, another part of thermal energy is converted to the atomic potential energy, as shown in Fig. 7. Similarly, the potential energy of liquid atom closing the substrate is raised, especially for the liquid atom on the groove region. The distributions of kinetic energy and potential energy indicate that the existence of a groove makes the liquid atoms on there obtain more thermal energy and tend to convert into a bubble nucleus. Even so, for the liquid atoms on the groove, the potential restriction is still much stronger than the kinetic energy during the initial stage of the nonequilibrium simulation process, as shown in Fig. 8. On the contrary, the kinetic energy is larger than potential restriction for the vapor atoms in the upper region. Therefore, more and more liquid atoms at the liquid-vapor interface evaporate into the upper vapor space.

With the heating process, the liquid atoms absorb more and more thermal energy from the heating substrate to increase their kinetic energy and weaken their potential restriction. As a result, the liquid atoms on the groove region obtain enough kinetic energy to break their potential restriction at about 4100 ps, as shown in Fig. 9(a). It is attractive that the position where the total energy larger than 0 eV coincides with the bubble nucleation position in Fig. 2(a), moreover, the incipient nucleation time shows the same consistency. Furthermore, once a bubble nucleus forms inside the liquid, the potential restriction on the liquid atoms at the interface of the bubble nucleus is significantly weakened, as shown in the potential energy contours of Fig. 9. Therefore, more and more liquid atoms at the interface of the bubble nucleus get rid of their potential restriction, and the region atomic kinetic energy larger than atomic potential restriction is enlarging, as shown in Fig. 9(b) and (c). As a result, the bubble nucleus keeps growing. Similarly, at the same time step, the shape of where total energy larger than 0 eV is almost the same as the bubble nucleus in Fig. 2. It noteworthy that the potential restriction on the argon atoms clinging to the substrate is always larger than their kinetic energy during the bubble nucleation process, which explains why a layer of solid-like argon atoms is restricted to the hydrophilic substrate surface all the time in the present study and the relevant researches [14–17].

The evolution of energy contours in Case A illustrates the availability of the “PK” norm in explaining the bubble nucleus formation on the hydrophilic grooved substrate. Moreover, to some extent, the classical heterogeneous nucleation theory about the liquid

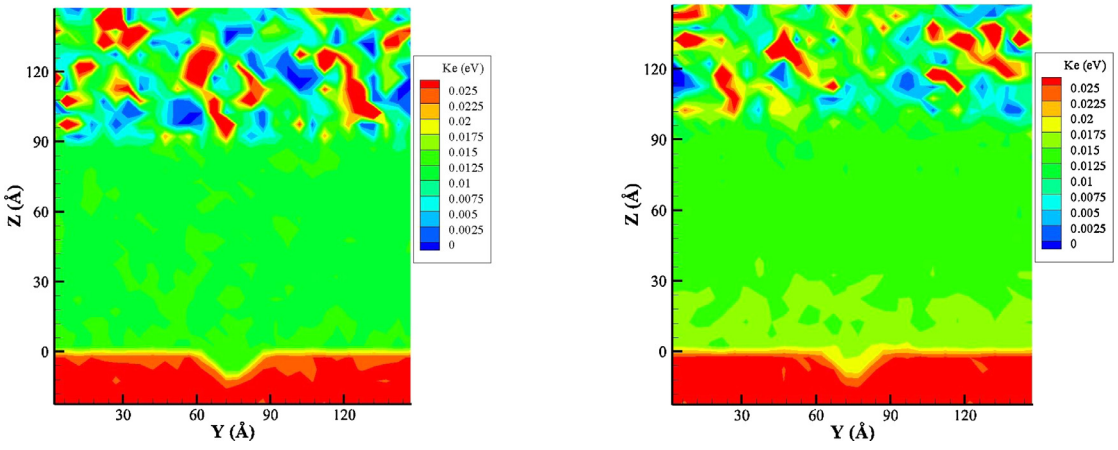

Fig. 6. The kinetic energy distribution in Case A during the initial stage of heating.

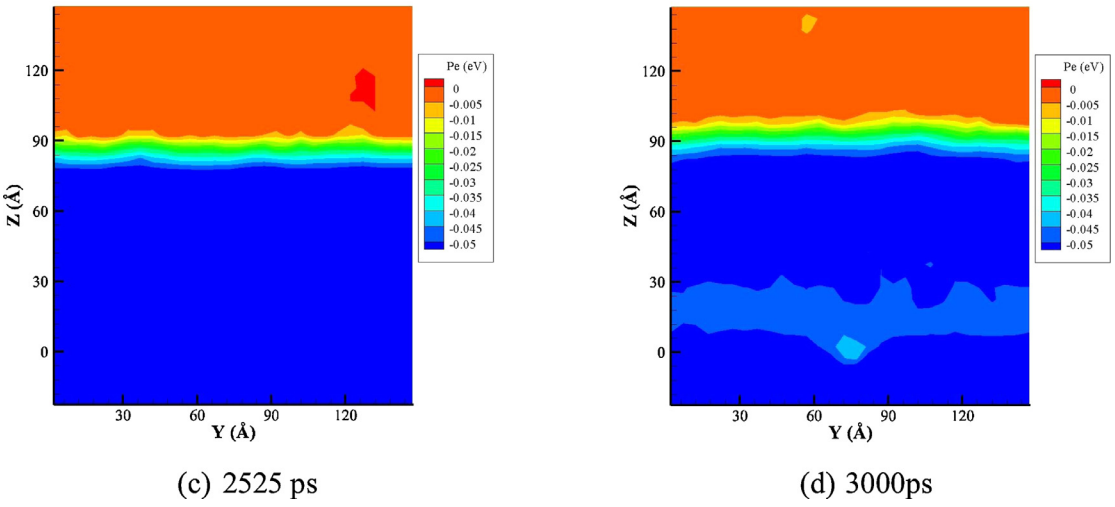

Fig. 7. The potential energy distribution in Case A during the initial stage of heating.

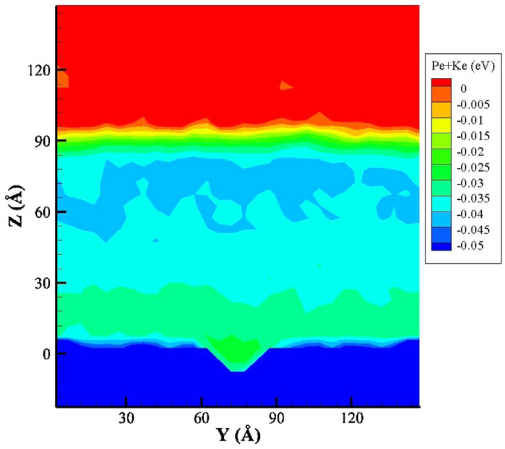

Fig. 8. The total energy distribution in Case A at 3000 ps.

on the groove region obtaining more thermal energy than that on the smooth region to achieve nucleating is verified as well.

3.4. The exploration of the reason for the strongly hydrophilic groove in shortening the incipient nucleation time

The groove hydrophilicity has significant effects on both heat transfer efficiency of solid-liquid and potential restriction on the liquid atoms, and to explain further the reason for the strongly hydrophilic groove in shortening the incipient nucleation time, the effects should be fully illustrated. The heat transfer efficiency of solid-liquid enhanced with the increase of substrate hydrophilicity has been shown in many studies [17], but the reason for that has not been reasonably explained. On the other hand, the relationship between substrate hydrophilicity and the potential restriction on liquid atoms has not been revealed as well. Therefore, in this subsection, the effects of hydrophilicity on the heat transfer efficiency of solid-liquid and potential restriction on the liquid argon are illustrated through a theoretical approach. Based on that, the reason for the strongly hydrophilic groove in shortening the incipient nucleation time is explained further.

The first is to calculate the potential restriction on liquid atoms. As shown in Fig. 10, an argon atom on the solid substrate is selected as the target atom. The calculation domain is a sphere with a radius of $R_{cut-off}$=12 Å, and the target atom is in the center of this sphere. The dark red region and light blue region represent liquid argon and metal platinum, respectively. The vertical distance between the target atom and the substrate surface is h. It is noteworthy that the minimum vertical distance $h_{\min}$ cannot be 0 because of the considerable interatomic repulsion. In the present study, $h_{\min}$ is set to 2.94 Å, which is the average value of σ_{Pt-Pt} and σ_{Ar-Ar}.

The potential restriction on liquid atoms changes with the nonequilibrium heating process because one part of thermal energy from the substrate is converted into the potential energy. However, at the initial moment of the nonequilibrium simulation stage, the density of argon liquid is approximately uniform under the equilibrium temperature of 90 K. Therefore, to simplify the derivation process and achieve the quantitative assessment of potential restriction for the cases with different wetting substrates, we assume the distribution of liquid atoms is uniform at the initial moment of the nonequilibrium simulation stage. The molecular number density of liquid argon and metal platinum are n_l and n_m, respectively. The details of the derivation process of potential restriction are illustrated as follows.

The total potential restriction on the target atom is shown as Eq. (11).

$$\Phi = \int\int\int_{V} \phi(r) n dV \tag{11}$$

where $\phi(r)$ and n represent L-J potential and molecular number density, respectively.

In the spherical coordinate system, the Eq. (11) is explained as follows.

$$\begin{aligned}\Phi = \int\int\int_{V} \phi(r) n \mathrm{d}v = n_l \int_{\theta_h}^{\pi} \mathrm{d}\theta \int_0^{2\pi} \mathrm{d}\varphi \int_{h_{\min}}^{-\frac{h}{\cos\theta}} \phi(r) r^2 \sin\theta \mathrm{d}r \\ + n_l \int_0^{\theta_h} \mathrm{d}\theta \int_0^{2\pi} \mathrm{d}\varphi \int_{h_{\min}}^{R_{\mathrm{cut-off}}} \phi(r) r^2 \sin\theta \mathrm{d}r + n_s \int_{\theta_h}^{\pi} \mathrm{d}\theta \int_0^{2\pi} \\ \times \mathrm{d}\varphi \int_{-\frac{h}{\cos\theta}}^{R_{\mathrm{cut-off}}} \phi(r) r^2 \sin\theta \mathrm{d}r\end{aligned} \tag{12}$$

Expand the first integral item on the right of the equal sign in Eq. (12):

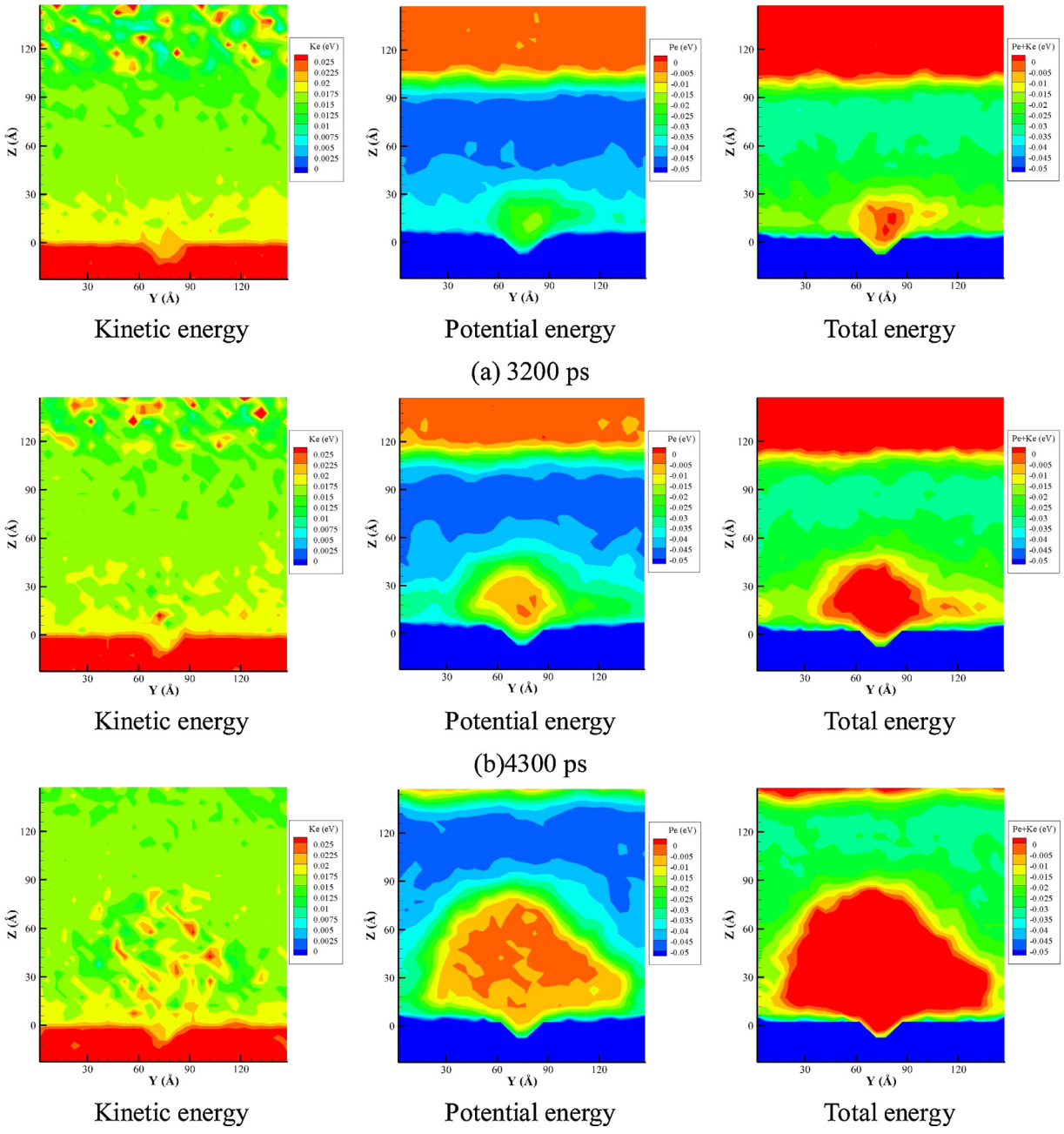

Fig. 9. The energy distributions in Case A at representative time steps.

$$
\begin{aligned}
& n_l \int_{\theta_h}^{\pi} \mathrm{d}\theta \int_0^{2\pi} \mathrm{d}\varphi \int_{h_{\min}}^{-\frac{h}{\cos\theta}} \phi(r) r^2 \sin\theta \mathrm{d}r \\
&= 2\pi n_l \int_{\theta_h}^{\pi} \sin\theta \mathrm{d}\theta \int_{h_{\min}}^{-\frac{h}{\cos\theta}} \phi(r) r^2 \mathrm{d}r \\
&= 2\pi n_l \int_{\theta_h}^{\pi} \sin\theta \left(-\frac{4\varepsilon_{\mathrm{Ar-Ar}}\sigma_{\mathrm{Ar-Ar}}{}^6}{3h^3}\cos^3\theta + \frac{4\varepsilon_{\mathrm{Ar-Ar}}\sigma_{\mathrm{Ar-Ar}}{}^{12}}{9h^9}\cos^9\theta - \frac{4\varepsilon_{\mathrm{Ar-Ar}}\sigma_{\mathrm{Ar-Ar}}{}^6}{3h_{\min}{}^3} + \frac{4\varepsilon_{\mathrm{Ar-Ar}}\sigma_{\mathrm{Ar-Ar}}{}^{12}}{9h_{\min}{}^9} \right) \mathrm{d}\theta \\
&= 2\pi n_l \int_{\pi}^{\theta_h} \left(-\frac{4\varepsilon_{\mathrm{Ar-Ar}}\sigma_{\mathrm{Ar-Ar}}{}^6}{3h^3}\cos^3\theta + \frac{4\varepsilon_{\mathrm{Ar-Ar}}\sigma_{\mathrm{Ar-Ar}}{}^{12}}{9h^9}\cos^9\theta - \frac{4\varepsilon_{\mathrm{Ar-Ar}}\sigma_{\mathrm{Ar-Ar}}{}^6}{3h_{\min}{}^3} + \frac{4\varepsilon_{\mathrm{Ar-Ar}}\sigma_{\mathrm{Ar-Ar}}{}^{12}}{9h_{\min}{}^9} \right) \mathrm{d}\cos\theta \\
&= 2\pi n_l \left[-\frac{\varepsilon_{\mathrm{Ar-Ar}}\sigma_{\mathrm{Ar-Ar}}{}^6}{3h^3}\cos^4\theta\Big|_{\pi}^{\theta_h} + \frac{2\varepsilon_{\mathrm{Ar-Ar}}\sigma_{\mathrm{Ar-Ar}}{}^{12}}{45h^9}\cos^{10}\theta\Big|_{\pi}^{\theta_h} + \left(\frac{4\varepsilon_{\mathrm{Ar-Ar}}\sigma_{\mathrm{Ar-Ar}}{}^{12}}{9h_{\min}{}^9} - \frac{4\varepsilon_{\mathrm{Ar-Ar}}\sigma_{\mathrm{Ar-Ar}}{}^6}{3h_{\min}{}^3} \right) \cos\theta\Big|_{\pi}^{\theta_h} \right] \\
&= \pi n_l \left[-\frac{\varepsilon_{\mathrm{Ar-Ar}}\sigma_{\mathrm{Ar-Ar}}{}^6}{3h^3}\left(\cos^4\theta_h - 1\right) + \frac{2\varepsilon_{\mathrm{Ar-Ar}}\sigma_{\mathrm{Ar-Ar}}{}^{12}}{45h^9}\left(\cos^{10}\theta_h - 1\right) + \left(\frac{4\varepsilon_{\mathrm{Ar-Ar}}\sigma_{\mathrm{Ar-Ar}}{}^{12}}{9h_{\min}{}^9} - \frac{4\varepsilon_{\mathrm{Ar-Ar}}\sigma_{\mathrm{Ar-Ar}}{}^6}{3h_{\min}{}^3} \right)\left(\cos\theta_h + 1\right) \right] \\
&= 2\pi n_l \left[\begin{array}{l} \dfrac{2\varepsilon_{\mathrm{Ar-Ar}}\sigma_{\mathrm{Ar-Ar}}{}^{12}}{45h^9}\cos^{10}\theta_h - \dfrac{\varepsilon_{\mathrm{Ar-Ar}}\sigma_{\mathrm{Ar-Ar}}{}^6}{3h^3}\cos^4\theta_h + \left(\dfrac{4\varepsilon_{\mathrm{Ar-Ar}}\sigma_{\mathrm{Ar-Ar}}{}^{12}}{9h_{\min}{}^9} - \dfrac{4\varepsilon_{\mathrm{Ar-Ar}}\sigma_{\mathrm{Ar-Ar}}{}^6}{3h_{\min}{}^3} \right)\cos\theta_h \\ \quad - \dfrac{2\varepsilon_{\mathrm{Ar-Ar}}\sigma_{\mathrm{Ar-Ar}}{}^{12}}{45h^9} + \dfrac{\varepsilon_{\mathrm{Ar-Ar}}\sigma_{\mathrm{Ar-Ar}}{}^6}{3h^3} + \dfrac{4\varepsilon_{\mathrm{Ar-Ar}}\sigma_{\mathrm{Ar-Ar}}{}^{12}}{9h_{\min}{}^9} - \dfrac{4\varepsilon_{\mathrm{Ar-Ar}}\sigma_{\mathrm{Ar-Ar}}{}^6}{3h_{\min}{}^3} \end{array} \right]
\end{aligned}
\tag{13}
$$

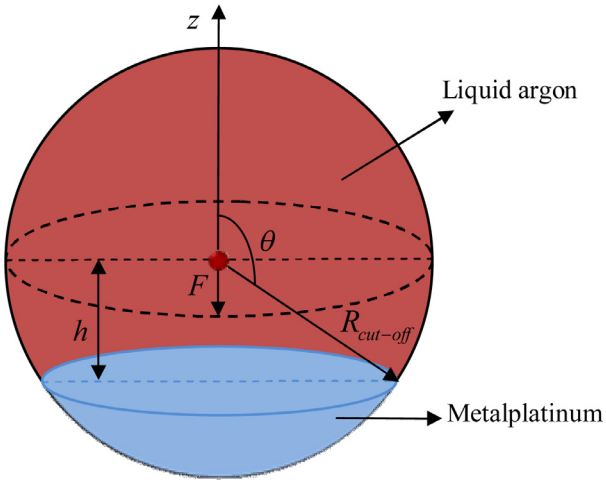

Fig. 10. calculation domain for calculating the vertical component of force on the target atom.

The same integration method is adopted to expand the remaining two terms on the right side of the equal sign in Eq. (12):

$$n_s\int_{\theta_h}^{\pi}\mathrm{d}\theta\int_0^{2\pi}\mathrm{d}\varphi\int_{-\frac{h}{\cos\theta}}^{R_{\mathrm{cut-off}}}\phi(r)r^2\sin\theta\,\mathrm{d}r$$
$$=2\pi n_s\left[\begin{array}{l}-\dfrac{2\varepsilon_{\mathrm{Ar-Pt}}\sigma_{\mathrm{Ar-Pt}}{}^{12}}{45h^9}\cos^{10}\theta_h+\dfrac{\varepsilon_{\mathrm{Ar-Pt}}\sigma_{\mathrm{Ar-Pt}}{}^{6}}{3h^3}\cos^4\theta_h\\ +\left(\dfrac{4\varepsilon_{\mathrm{Ar-Pt}}\sigma_{\mathrm{Ar-Pt}}{}^{6}}{3R_{cut-off}{}^{3}}-\dfrac{4\varepsilon_{\mathrm{Ar-Pt}}\sigma_{\mathrm{Ar-Pt}}{}^{12}}{9R_{cut-off}{}^{9}}\right)\cos\theta_h+\dfrac{4\varepsilon_{\mathrm{Ar-Pt}}\sigma_{\mathrm{Ar-Pt}}{}^{6}}{3R_{cut-off}{}^{3}}\\ -\dfrac{4\varepsilon_{\mathrm{Ar-Pt}}\sigma_{\mathrm{Ar-Pt}}{}^{12}}{9R_{cut-off}{}^{9}}-\dfrac{\varepsilon_{\mathrm{Ar-Pt}}\sigma_{\mathrm{Ar-Pt}}{}^{6}}{3h^3}+\dfrac{2\varepsilon_{\mathrm{Ar-Pt}}\sigma_{\mathrm{Ar-Pt}}{}^{12}}{45h^9}\end{array}\right]\tag{14}$$

$$n_l\int_0^{\theta_h}\mathrm{d}\theta\int_0^{2\pi}\mathrm{d}\varphi\int_{R_{\mathrm{min}}}^{R_{\mathrm{cut-off}}}\phi(r)r^2\sin\theta\,\mathrm{d}r$$
$$=2\pi n_l(1-\cos\theta_h)\left(\begin{array}{l}\dfrac{4\varepsilon_{\mathrm{Ar-Ar}}\sigma_{\mathrm{Ar-Ar}}{}^{6}}{3R_{\mathrm{cut-off}}{}^{3}}-\dfrac{4\varepsilon_{\mathrm{Ar-Ar}}\sigma_{\mathrm{Ar-Ar}}{}^{12}}{9R_{\mathrm{cut-off}}{}^{9}}\\ -\dfrac{4\varepsilon_{\mathrm{Ar-Ar}}\sigma_{\mathrm{Ar-Ar}}{}^{6}}{3R_{\mathrm{min}}{}^{3}}+\dfrac{4\varepsilon_{\mathrm{Ar-Ar}}\sigma_{\mathrm{Ar-Ar}}{}^{12}}{9R_{\mathrm{min}}{}^{9}}\end{array}\right)\tag{15}$$

The final expression of the total potential restriction on the target atom is obtained by substituting Eqs. (13), (14) and (15) into Eq. (12).

$$\Phi=\int_V\int\int\phi(r)n\mathrm{d}V$$
$$=2\pi n_l\left[\begin{array}{l}\left(\dfrac{\varepsilon_{\mathrm{Ar-Ar}}\sigma_{\mathrm{Ar-Ar}}{}^{6}}{R_{cut-off}{}^{4}}-\dfrac{2\varepsilon_{\mathrm{Ar-Ar}}\sigma_{\mathrm{Ar-Ar}}{}^{12}}{5R_{cut-off}{}^{10}}\right)h+\dfrac{\varepsilon_{\mathrm{Ar-Ar}}\sigma_{\mathrm{Ar-Ar}}{}^{6}}{3}h^{-3}\\ -\dfrac{2\varepsilon_{\mathrm{Ar-Ar}}\sigma_{\mathrm{Ar-Ar}}{}^{12}}{45}h^{-9}+\dfrac{8\varepsilon_{\mathrm{Ar-Ar}}\sigma_{\mathrm{Ar-Ar}}{}^{12}}{9R_{\mathrm{min}}{}^{9}}-\dfrac{8\varepsilon_{\mathrm{Ar-Ar}}\sigma_{\mathrm{Ar-Ar}}{}^{6}}{3R_{\mathrm{min}}{}^{3}}\\ +\dfrac{4\varepsilon_{\mathrm{Ar-Ar}}\sigma_{\mathrm{Ar-Ar}}{}^{6}}{3R_{\mathrm{cut-off}}{}^{3}}-\dfrac{4\varepsilon_{\mathrm{Ar-Ar}}\sigma_{\mathrm{Ar-Ar}}{}^{12}}{9R_{\mathrm{cut-off}}{}^{9}}\end{array}\right]$$
$$+2\pi n_s\left[\begin{array}{l}\left(\dfrac{2\varepsilon_{\mathrm{Ar-Pt}}\sigma_{\mathrm{Ar-Pt}}{}^{12}}{5R_{cut-off}{}^{10}}-\dfrac{\varepsilon_{\mathrm{Ar-Pt}}\sigma_{\mathrm{Ar-Pt}}{}^{6}}{R_{cut-off}{}^{4}}\right)h-\dfrac{\varepsilon_{\mathrm{Ar-Pt}}\sigma_{\mathrm{Ar-Pt}}{}^{6}}{3}h^{-3}\\ +\dfrac{2\varepsilon_{\mathrm{Ar-Pt}}\sigma_{\mathrm{Ar-Pt}}{}^{12}}{45}h^{-9}+\dfrac{4\varepsilon_{\mathrm{Ar-Pt}}\sigma_{\mathrm{Ar-Pt}}{}^{6}}{3R_{cut-off}{}^{3}}-\dfrac{4\varepsilon_{\mathrm{Ar-Pt}}\sigma_{\mathrm{Ar-Pt}}{}^{12}}{9R_{cut-off}{}^{9}}\end{array}\right]\tag{16}$$

Substitute the known parameters into Eq. (16), we can obtain the potential restriction on the target atom under different substrate hydrophilicity conditions, as shown in Fig. 11. It is evident

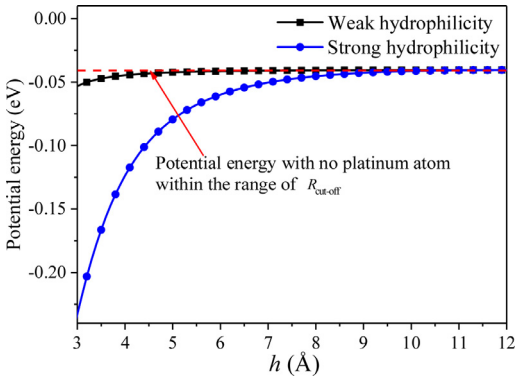

Fig. 11. Trends of potential restriction on target atom under different substrate hydrophilicity.

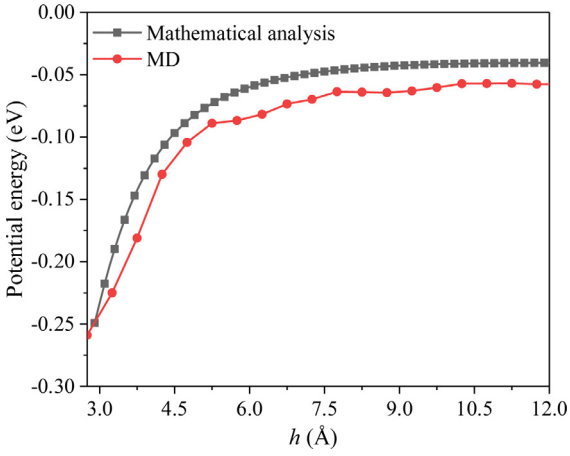

Fig. 12. Comparison between MD result and the mathematical analysis result in potential restriction.

that the argon atom in the vicinity of the substrate suffers a considerable potential restriction (negative value) from the surrounding atoms, and the magnitude of potential restriction increases with the enhancement of substrate hydrophilicity. Besides, the potential restriction quickly decreases with the increase of vertical distance h and closes to a fixed value, which is equal to potential restriction on the target atom without platinum atoms in the range of $R_{\mathrm{cut\text{-}off}}$. For the hydrophilic substrates, the potential restriction on the target atom reaches the peak when vertical distance h is 2.94 Å. Therefore, the reason for solid-like liquid atoms on the hydrophilic substrate surface is further verified by the mathematical method.

To verify the validity of the mathematical analysis results in potential restriction, a comparison between that and the MD result is made based on the strongly hydrophilic substrate, as shown in Fig. 12. There is no significant difference in the change trends of potential restriction between the MD result and the mathematical analysis result. Moreover, the average relative difference between them is 26.1%, which is tolerable considering some assumptions are made in the procedure of mathematical analysis.

The next is to obtain heat transfer efficiency of solid-liquid under different hydrophilicity. The thermal energy is transferred to the liquid from the heating substrate by the interatomic interaction, and the energy exchange efficiency can be heightened with the increase of the interaction probability. If the liquid atoms tend to approach the substrate surface, the probability of the solid-liquid interaction will be promoted. Therefore, the vertical component of force on the target argon atom is further calculated by

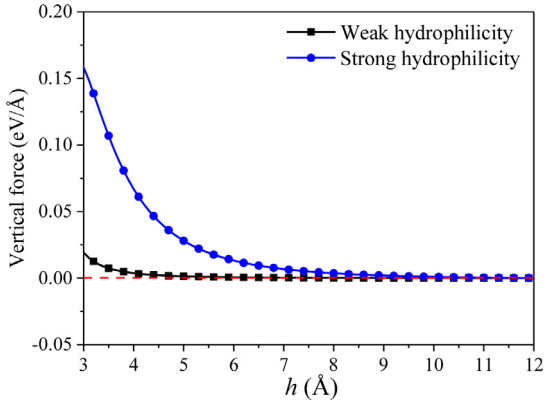

Fig. 13. Trends of vertical force on target atom under different substrate hydrophilicity conditions.

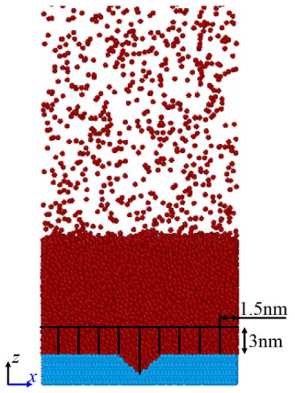

Fig. 14. Computational regions for obtaining transverse density and temperature profiles.

taking the derivative of Eq. (16).

$$F = -\frac{d\Phi}{dH} = 2\pi n_l \varepsilon_{Ar-Ar}\sigma_{Ar-Ar}{}^6\left[\left(\frac{2\sigma_{Ar-Ar}{}^6}{5R_{cut-off}{}^{10}} - \frac{1}{R_{cut-off}{}^4}\right) - \left(\frac{2\sigma_{Ar-Ar}{}^6}{5h^{10}} - \frac{1}{h^4}\right)\right] - 2\pi n_s \varepsilon_{Ar-Pt}\sigma_{Ar-Pt}{}^6\left[\left(\frac{2\sigma_{Ar-Pt}{}^6}{5R_{cut-off}{}^{10}} - \frac{1}{R_{cut-off}{}^4}\right) - \left(\frac{2\sigma_{Ar-Pt}{}^6}{5h^{10}} - \frac{1}{h^4}\right)\right] \quad (17)$$

Fig. 13 shows the vertical force with a downward direction on the target atom under different substrate hydrophilicity conditions. The vertical force on the target atom is bigger than 0 and becomes stronger with the enhancement of substrate hydrophilicity. Therefore, the liquid atoms tend to accumulate in the vicinity of the more hydrophilic substrate surface, and the corresponding probability of the metal-liquid interaction is promoted. Therefore, the heat transfer efficiency of solid-liquid is strengthened with the enhancement of substrate hydrophilicity.

To further quantitatively demonstrate the heat transfer efficiency difference between different hydrophilic substrates, the temperature and density profiles of liquid atoms near the grooved substrate and Kapitza resistance for different wetting substrates are obtained. The first is the temperature and density profiles of liquid atoms in the vicinity of the grooved substrate. A layer of argon film with a height of 30 Å clinging to the substrate surface is divided into 10 subregions with a width of 15 Å, as shown in Fig. 14. The density and temperature of each subregion are calculated at a regular time step to obtain the transverse density profile and temperature profile in both Cases A and B, respectively. It is noteworthy that the density profile is obtained at the initial moment of the nonequilibrium simulation stage because the heating process will affect the density comparison results. As shown

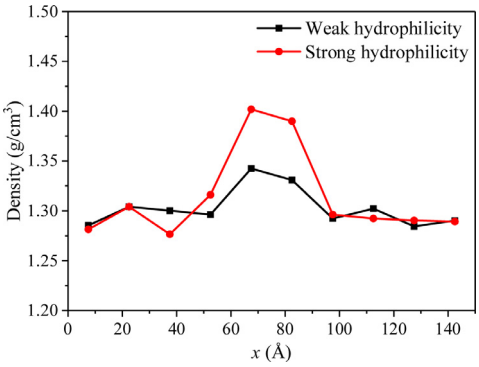

Fig. 15. Transverse density profile of argon film in the vicinity of the grooved substrate surface.

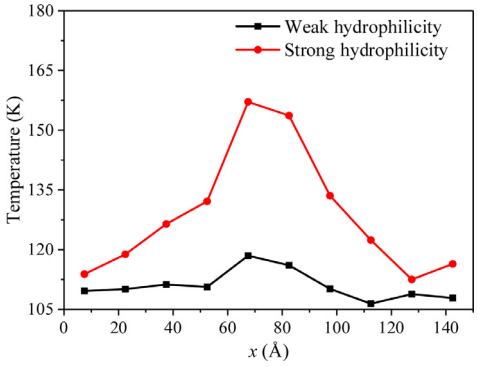

Fig. 16. Transverse temperature profile of argon film in the vicinity of the grooved substrate surface.

in Fig. 15, the transverse density profiles indicate that the argon atoms prefer to accumulate on the groove, especially on the strongly hydrophilic groove. Therefore, the probability of the thermal energy exchange through the liquid-metal interaction is large in the groove region. After a period of heating, the temperature of liquid on the groove region is higher than that on the smooth region at 2750 ps, and the strongly hydrophilic groove has a better performance in heat transfer, as shown in Fig. 16.

The next is the Kapitza resistance for different hydrophilic substrates. The Kapitza resistance is defined as follows [36]:

$$R_k = \frac{\Delta T_k}{q_k} \quad (18)$$

where ΔT_k is the temperature difference at the solid-liquid interface, and q_k is the heat flux through the solid-liquid interface.

To obtain the required parameters for the calculation of Kapitza resistance, a simulation system with a heat source and a heat sink is designed, as shown in Fig. 17. The controlling temperatures of the heat source and the heat sink are 96 K and 76 K, respectively. For the different wetting substrates, the accumulative energy flowing through the heat source is opposite to that flowing through the heat sink, as shown in Fig. 18. The slope of the accumulative energy flow curve is heat flux q_k, and the fitting results for the cases with different hydrophilic substrates are shown in Table 4. On the other hand, to obtain the temperature difference ΔT_k at the solid-liquid interface, the simulation box is divided into 44 slices with a thickness of 5 Å along the z-direction. The temperature of each slice is calculated every 100 time-steps and is averaged every 1000 time-steps. A steady longitudinal temperature profile of liquid is obtained after 5 ns simulation, as shown in Fig. 19. Based on the temperature profile, the temperature difference at the solid-liquid interface is obtained by linear extrapolation [37]. Finally, the Kapitza resistances for different hydrophilic substrates are easily

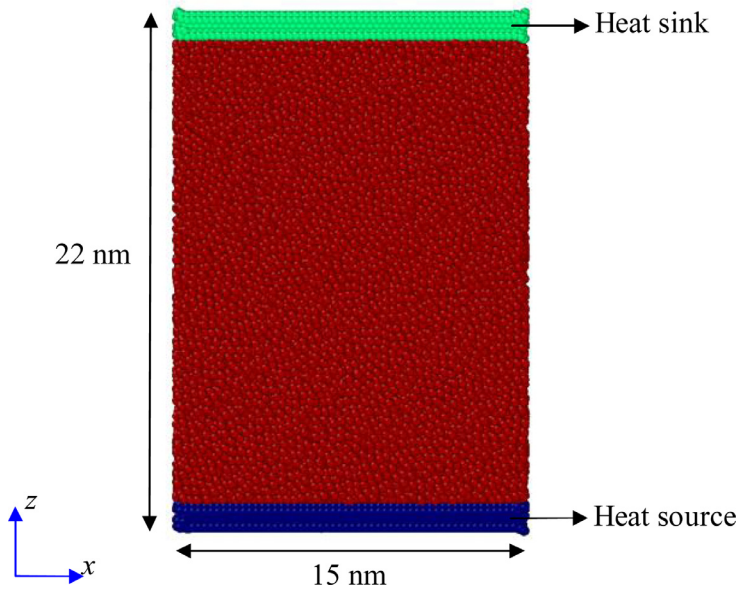

Fig. 17. Configuration of the simulation system for the calculation of Kapitza resistance.

Table 4
Interfacial thermal resistance for the different wettability systems

Wettability	Heat flux (10^6W/m^2)	Temperature difference (K)	Kapitza resistance (10^{-8}K• m^2/ W)
Strong hydrophilicity	96.72	1.83	1.89
Weak hydrophilicity	41.44	5.55	13.39

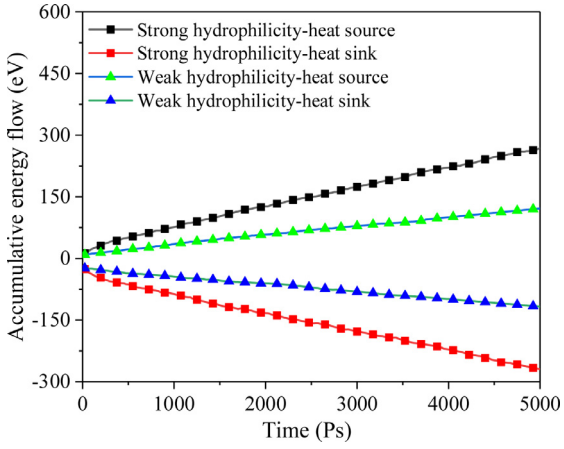

Fig. 18. Accumulative heat flows through heat source and heat sink for the cases with different hydrophilic substrates.

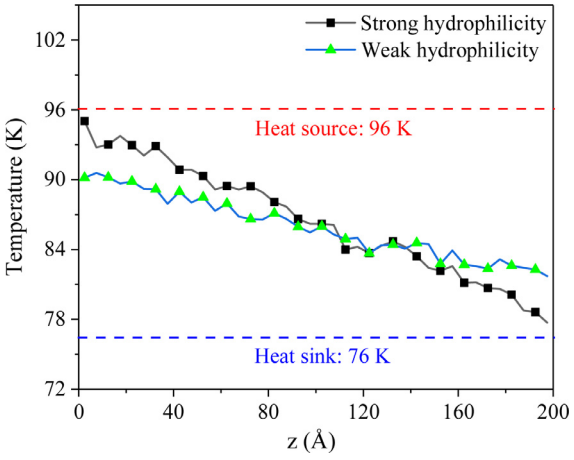

Fig. 19. Longitudinal temperature profiles of liquid for the cases with different hydrophilic substrates.

calculated by Eq. (18), and the results are listed in Table 4. The Kapitza resistance decreases with the enhancement of substrate hydrophilicity.

Based on the above analysis, we can find that both the heat transfer efficiency and the potential restriction on liquid atoms are improved with the enhancement of groove hydrophilicity. Therefore, the further comparison between atomic kinetic energy and atomic potential energy of liquid atoms on the strongly hydrophilic groove is needed. Fig. 20 illustrates the competition of atomic kinetic energy and atomic potential energy in Case B at 3000 ps. Compare with the kinetic energy contour in Fig. 6(b), the liquid atoms on the strongly hydrophilic groove obtain more kinetic energy than that on the weakly hydrophilic groove within the same time. Meanwhile, more thermal energy from the strongly hydrophilic groove is converted to decrease the potential restriction on the liquid atoms. Finally, the atomic kinetic energy wins the competition with the atomic potential restriction at about 3000 ps, leading the formation of a bubble nucleus on the groove, as shown in Fig. 20(c). On the other hand, the potential restriction on the liquid atoms from the strongly hydrophilic groove is so strong that more liquid atoms are limited in the groove after bubble nucleation.

In summary, both the heat transfer efficiency of solid-liquid and potential restriction on argon atom increase with substrate hydrophilicity, but the former wins the competition for the strongly hydrophilic groove. Therefore, for the hydrophilic substrate, with the increase of groove hydrophilicity, the incipient nucleation time is shortened, and the nucleation rate is improved.

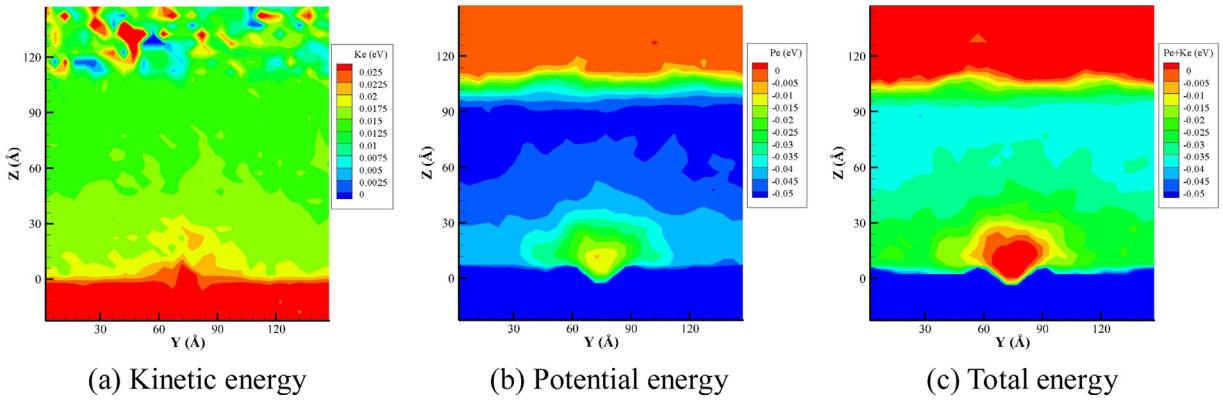

Fig. 20. The energy distributions in Case B at 3000 ps.

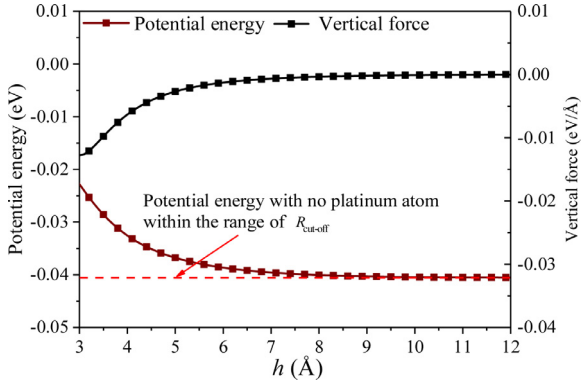

Fig. 21. The potential restriction and vertical force on the target atom in Case C.

3.5. The exploration of the reason for the residual gas in the strongly hydrophobic groove

The reason for the residual gas in the strongly hydrophobic groove has been preliminarily studied by the Lennard-Jones potential between two atoms in our previous study [17]. In the present study, the reason is explained further through the potential restriction and the vertical force on the target liquid atom discussed in Section 3.4. Substitute the parameters of the strongly hydrophobic substrate into Eqs. (16) and (17), we obtain the potential restriction and vertical force on the target argon atom, as shown in Fig. 21. The trends of both potential energy and vertical force in Case C are completely different from that in Cases A and B. For Case C, the potential restriction on the target liquid atom decreases with the decrease of solid-liquid distance *h*. Therefore, the liquid atoms tend to stay away from the strongly hydrophobic substrate to decrease their total energy. More importantly, the liquid atom suffers a repulsion from the strongly hydrophobic substrate, especially for the liquid atom closing to the substrate surface. As a result, it is hard for the liquid atoms to get into the strongly hydrophobic groove. Therefore, an initial bubble nucleus exists in the strongly hydrophobic groove at the beginning of the nonequilibrium heating stage.

On the other hand, the formation of the initial bubble nucleus can be further explained by the "PK" norm, as shown in Fig. 22. At the initial moment of the nonequilibrium stage, the kinetic energy of argon atoms is uniform. However, in the strongly hydrophobic groove region, the potential restriction on the argon atoms is so weak that some argon atoms can easily break it to form the initial bubble nucleus. In summary, to some extent, the classical heterogeneous nucleation theory about some residual gases in groove becoming the initial bubble nucleus is further explained in this subregion.

3.6. The exploration of the reason for the growth of the initial bubble nucleus from the strongly hydrophobic groove

The Kapitza resistance between liquid and the strongly hydrophobic substrate is 289.20 $\times$ 10^{-8} K•m^2/W, which is calculated by Eq. (18). Obviously, the initial bubble nucleus introduces a large thermal resistance, leading to the extremely inefficient heat transfer of solid-liquid in the strongly hydrophobic groove, as shown in Fig. 23. At 3000ps, the average kinetic energy of liquid atoms on the strongly hydrophobic groove region has little change by comparing the kinetic energy distribution in Fig. 22(a). Fortunately,

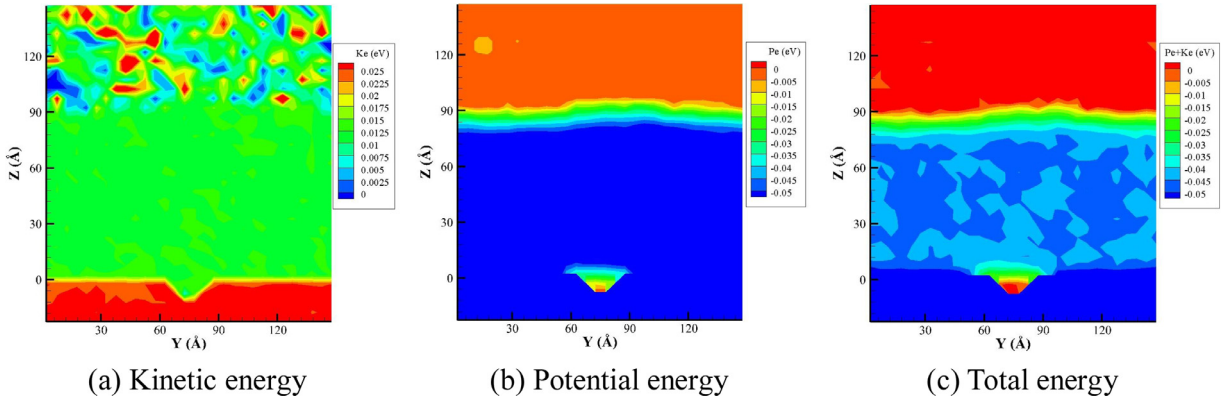

Fig. 22. The energy distributions in Case C at 2525 ps.

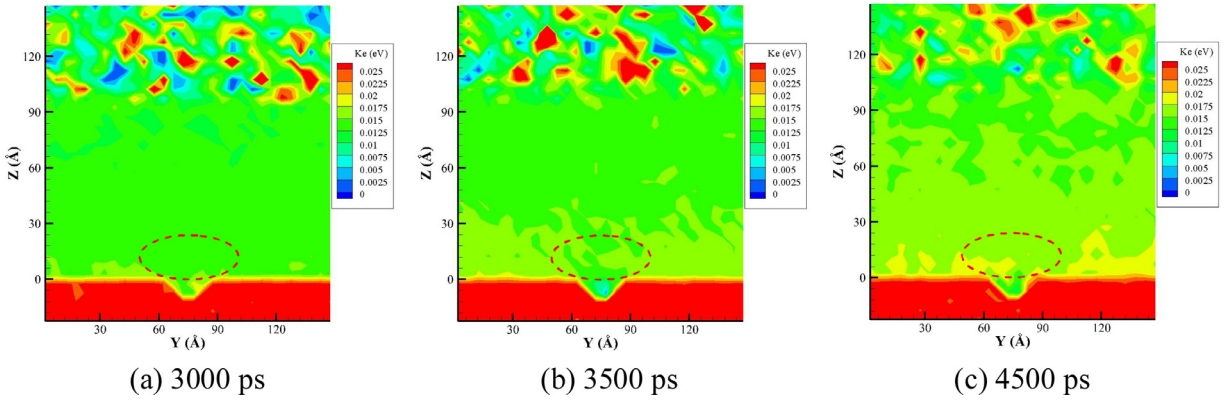

Fig. 23. The kinetic energy distribution in Case C at representative time steps.

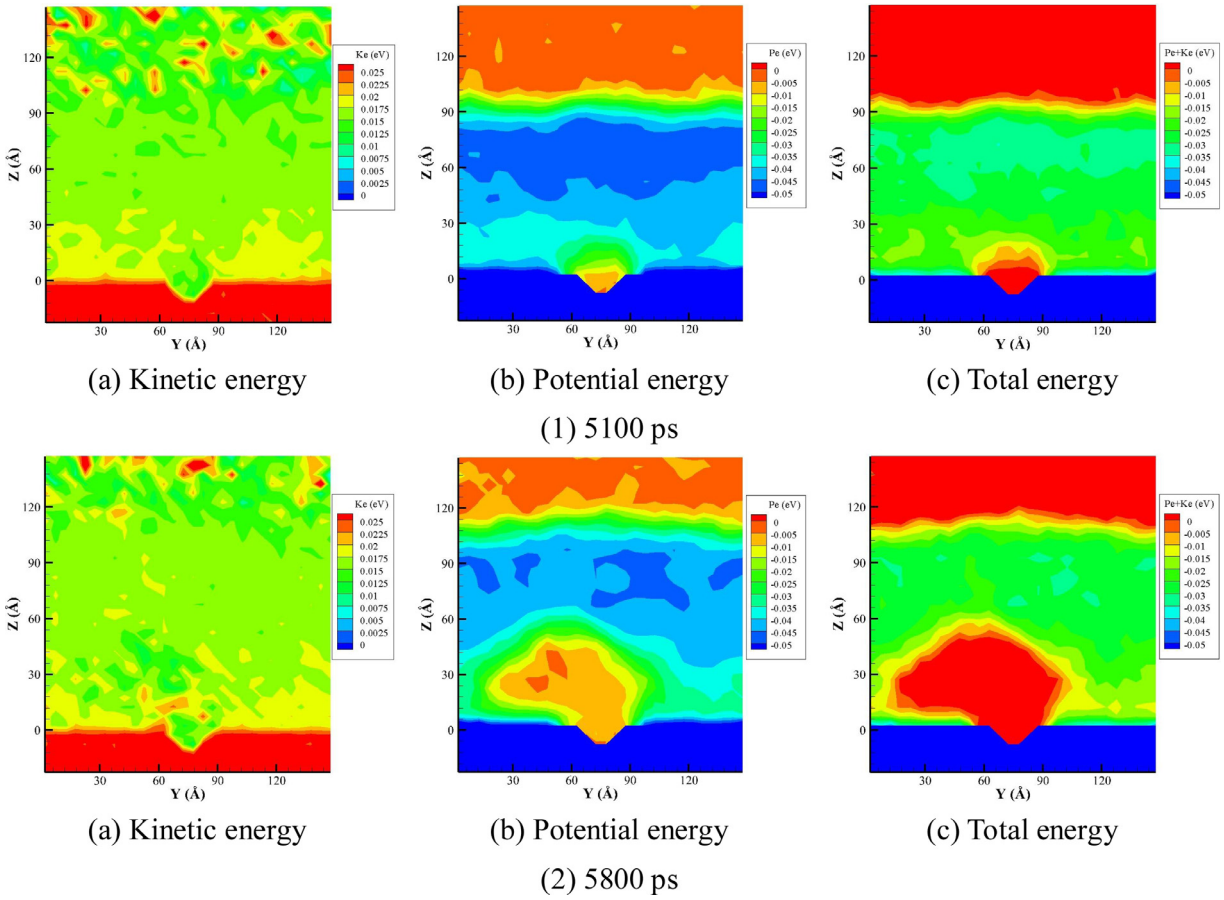

Fig. 24. The energy distributions in Case C at representative time steps.

the liquid atoms on the strongly hydrophobic groove can obtain thermal energy from the surrounding liquid atoms, which absorb thermal energy from the hydrophilic smooth regions, as shown in Figu. 23(b) and (c). As time goes on, the kinetic energy of liquid atoms on the strongly hydrophobic groove increases slowly and much higher than that inside the strongly hydrophobic groove.

Fig. 24 illustrates the distributions of kinetic energy, potential energy, and total energy in Case C at representative time steps. For the strongly hydrophobic groove, the weak potential restriction plays a dominant impact on the growth of the initial nucleus. Although the kinetic energy of liquid atoms on the strongly hydrophobic groove is smaller than that on the smooth hydrophilic region, more and more liquid atoms on the strongly hydrophobic groove break their weak potential restriction and become a part of the bubble nucleus. As a result, the initial bubble nucleus grows up from the groove with the heating process. The evolution of energy distributions in Case C indicates that the "PK" norm is still available to reveal the formation and growth mechanisms of a bubble nucleus on the strongly hydrophobic groove, although the effects of hydrophobic groove on bubble nucleation are completely different from that of the hydrophilic groove.

4. Conclusions

In this paper, the molecular dynamics simulation method is conducted to study the bubble nucleation phenomena on the grooved substrate with different wettability conditions. The availability of classical heterogeneous nucleation theory about the ef-

fects of groove on the bubble nucleus formation is verified, and the formation mechanism is further illustrated through the "PK" norm. The conclusions are summarized as follow:

(1) Different bubble nucleation phenomena happen on the grooved substrate with different wettability. A bubble nucleus generates from nothing on the hydrophilic groove, but where is covered by some solid-like liquid atoms all the time. On the contrary, some gases remain in the hydrophobic groove to form a stable initial bubble nucleus. These two different bubble nucleation phenomena are valuable to explore the formation mechanism of bubble nucleus on the grooved substrate from two perspectives of classical nucleation theory: the liquid in the groove obtaining more thermal energy to achieve nucleating and some residual gases in groove becoming the initial bubble nucleus.
(2) A "PK" norm is developed to illustrate the formation mechanism of the bubble nucleus on the grooved substrate. A group of liquid atoms in the simulation system has two types of energy: potential energy and kinetic energy. The potential energy relating to the density distribution limits the atomic movement, and the kinetic energy decided by the temperature indicates the atomic ability to move freely. If a group of atoms inside the liquid obtains enough kinetic energy to break their potential restriction, the bubble nucleation is happening.
(3) The classical nucleation theory about the liquid in the groove obtaining more thermal energy to achieve nucleating is verified by the "PK" norm. For the hydrophilic grooved substrate, the liquid atoms on the groove absorb more thermal energy than that on the smooth region within the same time. Some of the thermal energy is converted to increase atomic kinetic energy, and the other is converted to decrease atomic potential restriction. As a result, the liquid atoms on the hydrophilic groove obtain enough kinetic energy to break their potential restriction firstly, leading to the formation of a bubble nucleus.
(4) The classical nucleation theory about some residual gases in groove becoming the initial bubble nucleus is verified by the theoretical approach and "PK" norm. The liquid atom on the strongly hydrophobic groove suffers a large repulsion and weak potential restriction. Therefore, at the initial moment of nonequilibrium stage, some argon atoms on the strongly hydrophobic groove have got rid of their potential restriction and convert into an initial bubble nucleus without additional thermal energy.
(5) For the hydrophilic groove, the advantage of the strongly hydrophilic groove on bubble nucleation is revealed by the theoretical approach and "PK" norm. Both the heat transfer efficiency of solid-liquid and potential restriction on liquid atoms clinging to the substrate increase with the substrate hydrophilicity, but the former owns more advantages in the competition. Therefore, the liquid atoms on the strongly hydrophilic groove quickly obtain much kinetic energy to break their potential restriction and convert into a bubble nucleus in a short time.
(6) The reason for the growth of the initial bubble nucleus from the strongly hydrophobic groove is explained by the "PK" norm. On the contrary to the hydrophilic groove, the liquid atoms on the strongly hydrophobic groove are hard to absorb thermal energy from it because of considerable thermal resistance. Fortunately, the thermal energy from the surrounding liquid atoms helps them to get rid of the weak potential restriction and become a part of the bubble nucleus. As a result, the bubble nucleus grows up further from the strongly hydrophobic groove.
(7) The reason for the existence of solid-like liquid atoms on the hydrophilic substrate surface is revealed by the "PK" norm. The potential restriction from the hydrophilic substrate is so strong that a layer of liquid atoms is restricted on the substrate surface during the whole nonequilibrium simulation process.

Declaration of Competing Interest

None.

CRediT authorship contribution statement

Yu-Jie Chen: Methodology, Software, Data curation, Writing - original draft. **Bo Yu:** Validation, Methodology, Supervision, Conceptualization. **Yu Zou:** Conceptualization, Visualization. **Bing-Nan Chen:** Investigation, Visualization. **Wen-Quan Tao:** Writing - review & editing.

Acknowledgment

This work is supported by the National Natural Science Foundation of China (No. 51636006, No. 51606012), the Project of Construction of Innovative Teams and Teacher Career Development for Universities and Colleges under Beijing Municipality (IDHT20170507), and the Program of Great Wall Scholar (No. CIT&TCD20180313).

References

[1] J.H. Tsai, L. Lin, A thermal-bubble-actuated micronozzle-diffuser pump, J. Microelectromech. Syst. 11 (6) (2001) 665–671.
[2] H.Y. Kim, K.H. Jeong, S. Ko, et al., Life of thermal bubble on platinum microheater, J. Appl. Phys. 102 (3) (2007) 1041–1044.
[3] W. Wagner, A. Sokolow, R. Pearlstein, et al., Thermal vapor bubble and pressure dynamics during infrared laser ablation of tissue, Appl. Phys. Lett. 94 (1) (2009) 487.
[4] J.H. Tsai, L. Lin, A thermal-bubble-actuated micronozzle-diffuser pump, J. Microelectromech. Syst. 11 (6) (2001) 665–671.
[5] S. Chatpun, M. Watanabe, M. Shoji, Experimental study on characteristics of nucleate pool boiling by the effects of cavity arrangement, Exp. Therm. Fluid Sci. 29 (1) (2004) 33–40.
[6] S. Maruyama, Molecular dynamics methods in microscale heat transfer, Adv. Numer. Heat Transf. 47 (2002) 189–226.
[7] A. Hens, R. Agarwal, G. Biswas, Nanoscale study of boiling and evaporation in a liquid Ar film on a Pt heater using molecular dynamics simulation, Int. J. Heat Mass Transf. 71 (2014) 303–312.
[8] G. Nagayama, T. Tsuruta, P. Cheng, Molecular dynamics simulation on bubble formation in a nanochannel, Int. J. Heat Mass Transf. 49 (2006) 4437–4443.
[9] S. Maruyama, T. Kimura., A molecular dynamics simulation of bubble nucleation on solid surface, Nihon Kikai Gakkai Ronbunshu, B Hen/Transactions of the Japan Society of Mechanical Engineers, Part B 65 (1999) 3461–3467.
[10] T. Yamamoto, M. Matsumoto, Initial stage of nucleate boiling: molecular dynamics investigation, J. Therm. Sci. Technol. 7 (2012) 334–349.
[11] X. She, T.A. Shed, B. Lindeman, Y. Yin, X. Zhang, Bubble formation on solid surface with a groove based on molecular dynamics simulation, Int. J. Heat Mass Transf. 95 (2016) 278–287.
[12] Y. Liu, X. Zhang, Molecular dynamics simulation of nanobubble nucleation on rough surfaces, J. Chem. Phys. 146 (2017) 164704.
[13] W. Zhou, Y. Li, M. Li, J. Wei, W. Tao, Bubble nucleation over patterned surfaces with different wettability: molecular dynamics investigation, Int. J. Heat Mass Transf. 136 (2019) 1–9.
[14] Y. Chen, J. Li, B. Yu, D. Sun, Zou Y, D. Han, Nanoscale study of bubble nucleation on a grooved substrate using molecular dynamics simulation, Langmuir 34 (2018) 14234–14248.
[15] Y. Chen, Y. Zou, D. Sun, Y. Wang, B. Yu, Molecular dynamics simulation of bubble nucleation on nanostructure surface, Int. J. Heat Mass Transf. 118 (2018) 1143–1151.
[16] Y. Chen, Y. Zou, Y. Wang, D. Han, B. Yu, Bubble nucleation on various surfaces with inhomogeneous interface wettability based on molecular dynamics simulation, Int. Commun. Heat Mass Transf. 98 (2018) 135–142.
[17] Y. Chen, Y. Zou, B. Yu, D. Sun, X. Chen, Effects of surface wettability on rapid boiling and bubble nucleation: a molecular dynamics study, Nanoscale Microscale Thermophys. Eng. 22 (2018) 198–212.
[18] S. Yang, W. Tao, Heat Transfer, Higher Education Press, 2006 Chap VI.
[19] V.K. Shen, P.G. Debenedetti, A kinetic theory of homogeneous bubble nucleation, J. Chem. Phys. 118 (2003) 768–782.
[20] H.R. Seyf, Y. Zhang, Effect of nanotextured array of conical features on explosive boiling over a flat substrate: a nonequilibrium molecular dynamics study, Int. J. Heat Mass Transf. 66 (2013) 613–624.
[21] G. Nagayama, P. Cheng, Effects of interface wettability on microscale flow by molecular dynamics simulation, Int. J. Heat Mass Transf. 47 (2004) 501–513.

[22] X.D. Din, E.E. Michaelides, Kinetic theory and molecular dynamics simulations of microscopic flows, Phys. Fluids 9 (1997) 3915–3925.
[23] J.L. Barrat, L. Bocquet, Large slip effect at a nonwetting fluid-solid interface, Phys. Rev. Lett. 82 (1999) 4671–4674.
[24] J. Delhommelle, P. Millie, Inadequacy of the Lorentz–Berthelot combining rules for accurate predictions of equilibrium properties by molecular simulation, Mol. Phys. 99 (2001) 619–625.
[25] S. Plimpton, Fast parallel algorithms for short-range molecular dynamics, J. Comput. Phys. 117 (1993) 1–19.
[26] M.P. Allen, D.J. Tildesley, J.R. Banavar, Computer Simulation of Liquids, Oxford Unicersity Press, New York, 1987.
[27] A. Stukowski, Visualization and analysis of atomistic simulation data with ovito-the open visualization tool, Model. Simul. Mater. Sci. Eng. 18 (2010) 2154–2162.
[28] S.M. Shavik, M.N. Hasan, A.K.M.M. Morshed, M.Q. Islam, Molecular dynamics study of effect of different wetting conditions on evaporation and explosive boiling of ultra-thin argon layer over platinum surface, Procedia Eng. 105 (2015) 446–451.
[29] P. Hänggi, P. Talkner, M. Borkovec, Rev. Mod. Phys. 62 (1990) 251.
[30] R. Zwanzig, Nonequilibrium Statistical Mechanics, Oxford University Press, Oxford, 2001.
[31] J. Wedekind, R. Strey, D. Reguera, New method to analyze simulations of activated processes, J. Chem. Phys. 126 (2007) 134103.
[32] J. Frenkel, Kinetic Theory of Liquids, Clarendon, Oxford, 1946 Chap.VII.
[33] J. Wedekind, D. Reguera, Kinetic reconstruction of the free-energy landscape, J. Phys. Chem. B 112 (2008) 11060.
[34] V.G. Baidakov, K.S. Bobrov, Spontaneous cavitation in a Lennard-Jones liquid at negative pressures, J. Chem. Phys. 140 (2014) 184506.
[35] T.L. Hill, Molecular clusters in imperfect gases, J. Chem. Phys. 23 (1955) 617.
[36] Q. Cao, Z. Cui, Molecular dynamics simulations of the effect of surface wettability on nanoscale liquid film phase-change, Numer. Heat Transf., Part A 75 (2019) 533–547.
[37] H. Acharya, N.J. Mozdzierz, P. Keblinski, S. Garde, How chemistry, nanoscale roughness, and the direction of heat flow affect thermal conductance of solid–water interfaces, Ind. Eng. Chem. Res. 51 (2012) 1767–1773.